Mechanisms of Structural Reordering During Thermal Transformation of Aluminogermanate Imogolite Nanotubes

Geoffrey Monet, Stéphan Rouzière, Delphine Vantelon, Cristina Coelho Diogo, David Maurin, Jean-Louis Bantignies, Pascale Launois, Erwan Paineau

HAL Id: hal-03278914
https://hal.science/hal-03278914

Mechanisms of Structural Reordering During Thermal Transformation of Aluminogermanate Imogolite Nanotubes

Geoffrey Monet,[†] Stéphan Rouzière,[†] Delphine Vantelon,[‡] Cristina Coelho Diogo,[¶] David Maurin,[§] Jean-Louis Bantignies,[§] Pascale Launois,[*,†] and Erwan Paineau[*,†]

[†]*Université Paris-Saclay, CNRS, Laboratoire de Physique des Solides, F-91405, Orsay, France*
[‡]*Synchrotron SOLEIL, L'orme des Merisiers, Saint-Aubin, BP 48, 91192 Gif-sur-Yvette Cedex, France*
[¶]*Sorbonne-Université, CNRS, Institut des Matériaux de Paris-Centre, FR2482, F-75005, Paris, France*
[§]*Laboratoire Charles Coulomb, UMR 5221 CNRS-Université de Montpellier, F-34095 Montpellier, France*

E-mail: pascale.launois@universite-paris-saclay.fr; erwan-nicolas.paineau@universite-paris-saclay.fr

Abstract

Metal oxide aluminosilicate and aluminogermanate nanotubes, called imogolite nanotubes, are custom made nanotubes with controlled diameter, morphology and organization. These nanotubes undergo major structural changes at high temperatures. Here, we report a complete analysis of the structural transformation of single and double-walled aluminogermanate nanotubes, organized or not in bundles, up to 800 °C. Complementary X-ray scattering and spectroscopy experiments were performed. The evolution of both Al and Ge atoms coordination during the transformation process was studied in-situ. Quantitative analysis of X-ray absorption spectra reveals that the dehydroxylation of nanotubes leads to intermediate stages of 'metaimogolite', which differ in the coordination of the aluminium atoms. A mechanism explaining the major structural reorganization is proposed based on atomic jump processes.

Introduction

Thermal treatment is one of the most commonly applied process to modify the structure, porosity and surface reactivity properties of aluminosilicate clay minerals. The structural transformation of these materials with temperature is usually split into three phases:[1] (*i*) dehydration stage, (*ii*) dehydroxylation stage coupled with a significant modification of the crystalline structure and (*iii*) long-distance atomic re-organization and re-crystallization.

During the dehydroxylation stage, clay materials may proceed through intermediate and metastable stages, whose structure is sometimes only partially known even now. For instance, dehydroxylation of kaolinite, a dioctahedral clay mineral, induces the formation of metakaolin,[2–5] which has valuable properties for catalysis,[6] as binder in lightweight cements and concretes,[7] or as precursor for zeolite synthesis.[8,9] The formation of such intermediate phase is not limited to two-dimensional aluminosilicate clays. Similar structural evolution have

1

been reported during heat treatment of halloysite nanotubes (rolled kaolinite sheet)[5,10,11] and allophane nanospheres.[12] Transformation into crystalline mullite is observed at high temperature.[2,4,11,12]

A very peculiar clay nanomaterial is imogolite. Imogolite nanotubes (INTs) were first discovered in soils.[13] They are also readily synthesized with well-controlled diameter, adjustable morphology and rationally designed interface and organization.[14–23] These $(OH)_3Al_2O_3X(R)$ (with X = Si or Ge; R = OH, CH_3...) nanotubes are made of isolated tetrahedral $[(R)XO_3]$ units on the inner surface connected to a curved gibbsite-like octahedral framework on the outer surface $[Al(OH)_3]$.[22,24,25] They can form either individual single- (SW) or double-walled (DW) nanotubes of few nanometers in diameter (Figure 1).[26,27] In other clay nanomaterials such as kaolinite or halloysite, polymerized SiO_4 tetrahedra form an interconnected layer with apical oxygen connected to the octahedral layer while they are isolated and inverted in imogolite structure. Tetrahedron orientation in INTs is thus exceptional for a clay mineral.
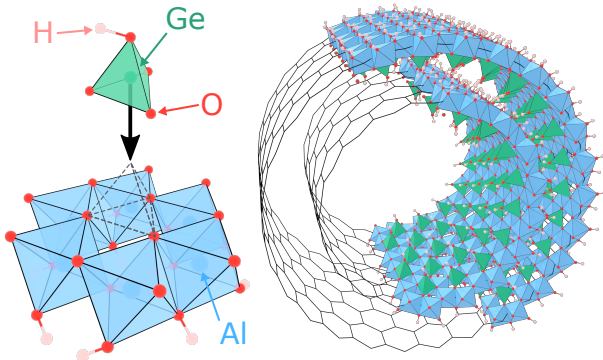

Figure 1: Polyhedral representation of a double-walled Ge-INT where $O_3Al(OH)_3$ blue octahedra are arranged to form a honeycomb network and green O_3GeOH tetrahedra are placed right above each octahedral cavity.

The thermal stability of imogolite nanotubes has been addressed extensively since their discovery,[28] highlighting the expected phase sequence with dehydration around $T \sim 120\,°C$ then dehydroxylation ($T = 300 - 500\,°C$) of the nanotubes before transformation into mullite for temperatures above $900\,°C$.[13,29] Like other clay nanomaterials, these nanotubes undergo major structural transformations during dehydroxylation stage. An amorphous phase was observed from X-ray scattering experiments on INT samples thermally treated at $350\,°C$[30] or around $500\,°C$,[29] related to a probable collapse of the nanotube structure.[31] Some studies proposed a mechanism based on the breakage of the nanotubes and the formation of a layer structure,[32] in which however residual tubular structures could be retained.[33] At a local level, solid-state nuclear magnetic resonance (NMR) experiments and density functional theory (DFT) simulations hinted important local modification of Al coordination,[34,35] together with a cross-linking of Si tetrahedral sites.[36,37] But a unified description of the thermally induced reorganization based on the whole set of available experimental data is still missing to date.

The interest of a 'metaimogolite' phase with appealing properties as those reported for metakaolinites or metahalloysites,[38,39] has led us to re-examine the effect of temperature on INTs. Most studies on the thermal transformation of imogolite nanotubes were performed on aluminosilicate INTs. Here, we focus on aluminogermanate analogues (Ge-INTs) because they can be synthesized (i) in large quantities,[40] (ii) with one (SW Ge-INTs) or two walls (DW Ge-INTs)[26] (iii) while controlling their organization as isolated or bundled nanotubes.[41,42] We propose in this article a complete analysis of the thermally-induced structural changes of Ge-INTs. The evolution of the long-distance structure was investigated by in-situ and ex-situ X-ray scattering measurements. To go beyond, we applied an original approach including in-situ flyscan X-ray absorption (XAS) spectroscopy measurements, allowing us to follow the changes of both Al and Ge atoms coordination during the transformation process. Altogether, we evidence that from dehydration of the nanotube to its recrystallization in mullite form, the structure goes through three intermediate stages (stages I, II, III) for which the coordination of the aluminum atoms differs. In particular, we propose an original model based on atomic jump processes to explain the atomic rearrangement after dehydrox-

ylation.

Materials and Methods

Chemicals

Aluminum perchlorate nonahydrate (Al-$ClO_3.9H_2O$, ACS reagent, $\geq$ 98 %), anhydrous NaOH (ACS reagent, $\geq$ 97 %), urea $(CO(NH_2)_2$, ACS reagent, $\geq$ 99 %) and tetraethoxygermanium (TEOG, $Ge(OC_2H_5)_4$, ACS reagent, $\geq$ 99.5 %) were purchased from Sigma Aldrich. KBr (IR grade) was purchased from Merck. All products were used as received.

Nanotube syntheses

Aluminogermanate INTs were synthesized by the co-precipitation under vigorous stirring of an aluminum perchlorate solution and TEOG with an [Al]/[Ge] ratio of 2. SW Ge-INTs were synthesized with an initial aluminum concentration of $C_{Al} = 1$ mol.L^{-1}, followed by slow hydrolysis through the addition of a NaOH solution (1 mol.L^{-1}) until a hydrolysis ratio $R_{[OH]/[Al]}$ of 2 is reached. The mixture was then aged for 5 days into an oven at 95 °C.[43] For DW Ge-INTs, a single-step procedure was applied as described elsewhere.[40] In that case, TEOG was mixed together with an aluminum perchlorate solution $(C_{Al} = 0.2$ mol.$L^{-1})$ and a urea solution up to a [urea]/[Al] ratio of 1. The mixture was transferred in an autoclave and placed in an oven at 140 °C for 5 days.

Samples preparation

Suspensions were recovered at room temperature and subsequently dialyzed against ultrapure water (Spectra/Por, cut-off 10 kDa, Spectrum). Similar INTs samples have been characterized in our previous works, showing that both type of INTs have monodisperse diameters of 4.1 (SW) and 4.3 nm (DW) (one reports here their external diameters).[43,44] The degree of nanotube organization can be easily controlled by varying the number of dialysis steps x.[41] For each nanotube morphology, two sets of suspensions have been prepared: (i)

$x = 4$ to obtain imogolite bundles. These samples will be referred as SW_b and DW_b in the following. (ii) $x = 9$ for fully dispersed SW or DW Ge-INTs. The four suspensions were left to evaporate at room temperature during one week in polystyrene weighing dishes to get self-supported films.[45] A part of the obtained films were stored as such for in-situ synchrotron-based experiments while the rest was milled in an agate mortar to obtain a fine powder.

Thermogravimetric analyses (TGA) were carried out (TGA Q50, TA Instruments) by heating 20 mg of powder sample under N_2 gas flux with a temperature ramp of 10 °C.min^{-1}.[46]

Series of powder samples were annealed in quartz crucibles at defined temperature (300, 400, 500, 600, 700, 800, 900 and 1000 °C) for 2 h in a muffle furnace (Thermolyne Furnace 6000) under air atmosphere prior to use for ex-situ experiments performed at room temperature.

Ex-situ experiments

Wide-Angle X-ray scattering

Powder samples were filled into borosilicate capillary tubes (WJM-Glas/Müller GmbH, DE) of 1 mm diameter and flame-sealed. Wide-Angle X-ray scattering (WAXS) measurements were carried out on a Cu rotating anode generator (Rigaku, Corporation, Japan), providing a monochromatic beam with incident wavelength $\lambda = 1.5418$ Å after confocal parabolic W/Si multilayer mirrors. Experiments were performed in a vacuum chamber to optimize the signal over background ratio. The scattered intensity was collected on a large cylindrical image plate placed at a sample-to-detector distance of 104.8 mm. Pixels counts were angularly summed and intensity versus wave-vector Q curves were thus obtained ($Q = 4\pi/\lambda \sin\theta$, where 2θ is the scattering angle). Values as large as $Q = 8$ Å^{-1} are reached. Intensity is corrected for polarization and geometrical factors.

Infrared spectroscopy

Fourier transform infrared (FT-IR) spectroscopy measurements were performed using

a Bruker Tensor 27 spectrometer. The measurements were performed in the mid-infrared region $(400 - 4000 \, \text{cm}^{-1})$ in the transmission configuration using KBr pellets ($\sim 1.3 \, \text{mg}$ powder INT sample$/300 \, \text{mg}$ KBr), prepared under 7-tons pressure. Prior to IR experiments, the pellets were dried at $100 \, °\text{C}$ for about $20 \, \text{h}$, to reduce the levels of adsorbed water. The IR spectra were collected at room temperature by averaging 128 scans with a spectral resolution of $4 \, \text{cm}^{-1}$.

Nuclear Magnetic Resonance

Solid-state magic-angle spinning (MAS) NMR experiments were performed on a Bruker AVANCE III 700 spectrometer based on a $16.4 \, \text{T}$ superconducting solenoid operating at $\nu_0(^{27}\text{Al}) = 182.47 \, \text{MHz}$ using commercial double resonance Bruker MAS probes. Powder samples prepared at room temperature and at $\text{T} = 800 \, °\text{C}$ were transferred to ZrO_2 rotors with an outer diameter of $2.5 \, \text{mm}$ and were heated at $200 \, °\text{C}$ to remove adsorbed water. For measurements, the rotors were spinned at a MAS rate of $25 \, \text{kHz}$. All ^{27}Al (spin $l = 5/2$) MAS NMR spectra were obtained by using short pulses ($< \pi/8$) for quantitative purposes. Nutation curves were first established by using a solution of 1M $Al(NO_3)_3$. All decomposition of spectra were performed using the DMfit software.[47]

In-situ synchrotron-based experiments

Combined in-situ X-ray scattering (XRS) and X-ray absorption spectroscopy (XAS) experiments were carried out on the DiffAbs beamline at the synchrotron SOLEIL. The experiments were performed at the Ge K-edge ($E_0 = 11.1 \, \text{keV}$) using a Si(111) double crystal monochromator. Film samples were mounted in a furnace (DHS900, Anton Paar GmbH) operating in air from room temperature to $700 \, °\text{C}$. XRS measurements were first performed in a continuous way (flyScan mode), at a heating rate of $2 \, °\text{C.min}^{-1}$, up to temperature steps at which XAS measurements were performed. A CCD camera (SX- 165 model, Rayonix, USA)

was used to measure XRS patterns in the Q-range $[0.1 - 4 \, \text{Å}^{-1}]$, in reflection geometry (vertical sample surface). A SDD detector allowed recording XAS spectra in fluorescence mode within the same experimental setup configuration. Extended X-ray absorption fine structure (EXAFS) oscillations were extracted after standard procedures using the ATHENA software package,[48] and were compared to simulations performed with the IFEFFIT code[48].

X-ray absorption spectra at the Al K-edge were collected at the LUCIA beamline of synchrotron SOLEIL.[49] The X-ray beam was monochromatised with a KTP(011) double crystal and beam focalization was ensured by Kirkpatrick-Baez mirrors, allowing a beam size of $3 \times 3 \, \text{µm}^2$ on the sample. The energy of the monochromator was calibrated on the first peak of the first derivative of an Al foil spectrum at $1559.6 \, \text{eV}$. INT film samples were placed in a primary vacuum chamber equipped with a dedicated home-made oven. XANES measurements were performed by collecting the fluorescence spectra continuously while increasing the temperature until $800 \, °\text{C}$, with a ramp of $5 \, °\text{C.min}^{-1}$. XANES spectra range from $1550 \, \text{eV}$ to $1700 \, \text{eV}$ with an energy step of $0.2 \, \text{eV}$ and a counting time of $0.3 \, \text{s}$. Moreover, in order to highlight the kinetics of the transformation, constant temperature stages have been made at 500, 700 and $800 \, °\text{C}$ where data were collected for about 1 hour. XANES data were obtained after performing standard procedures for pre-edge subtraction, normalization and self-absorption correction using the ATHENA software package.[48] The fit of the XANES curves was done on the $1560 - 1580 \, \text{eV}$ region using the Python lmfit library.[50]

Results and discussion

We performed the experiments on four different samples (SW or DW nanotubes, isolated or in bundles). However, results were quite close. Thus only the results obtained for DW nanotubes are presented in the main part of the article, the others data being provided in Supplementary Information.
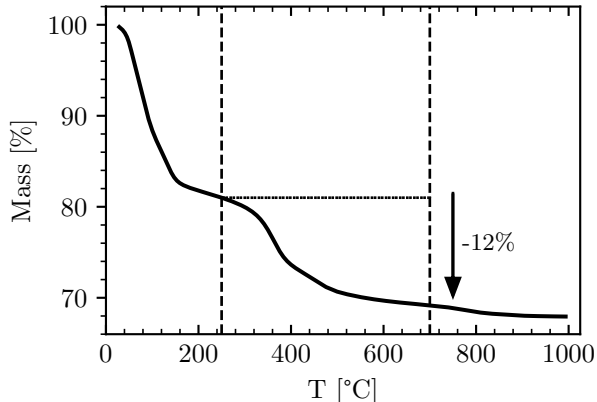
Thermogravimetric analysis

Figure 2: Typical TGA curve obtained for a powder of DW INTs.

Mass loss of DW sample as a function of temperature is shown in Figure 2. All samples (SW, SW$_b$, DW and DW$_b$) present similar TGA curves (Figure S1). The first mass loss, below 200 °C, is due to the desorption of water loaded inside and between aluminogermanate nanotubes walls.[43,51,52] A second mass loss is evidenced between 300 and 500 °C, which we mainly attribute to the dehydroxylation of the INT structure.[33,51] Indeed, corresponding mass losses, calculated as the difference between masses at 250 °C and 700 °C normalized to the mass at 700 °C, are found to be equal to 12 %, 13 %, 11 % and 10 % for DW, DW$_b$, SW and SW$_b$ samples respectively. Thermal decomposition of remaining perchlorate ions of the starting precursors used in the synthesis occurs in the same temperature range,[33] but their contribution remains negligible. Indeed, the dehydroxylation relation GeAl$_2$O$_7$H$_4$ $\longrightarrow$ GeAl$_2$O$_5$ + 2 H$_2$O leads to a mass loss of 15 % after the release of water molecules. Our measured mass losses thus appear compatible with a complete dehydroxylation process, similar to the one observed in kaolinite or halloysite.[2,4,11] The dehydroxylation process of imogolite can be split into a part corresponding to the outer wall (OH)$_3$Al$_2$O$_{1.5}$ $\longrightarrow$ O$_{1.5}$Al$_2$O$_{1.5}$ + 1.5 H$_2$O, and to the inner wall O$_{1.5}$Ge(OH) $\longrightarrow$ O$_{1.5}$GeO$_{0.5}$ + 0.5 H$_2$O of the nanotube. Thus, the dehydroxylation quanti-

fied by the TGA will result in a loss of 1.5 external and 0.5 internal OH groups. Presumably, this would be associated with the formation of Ge-O-Ge bridging to maintain 4 oxygens around the germanium atoms as it has been shown for silicium-based imogolite nanotubes.[34]

Phase transformation in mullite-type compound

X-ray scattering is a powerful tool for investigating the structure of imogolite nanotubes.[22] Figure 3 and Figure S2 present the evolution of the WAXS diagrams of powder samples of DW and SW INTs, annealed ex-situ up to 1000°C.
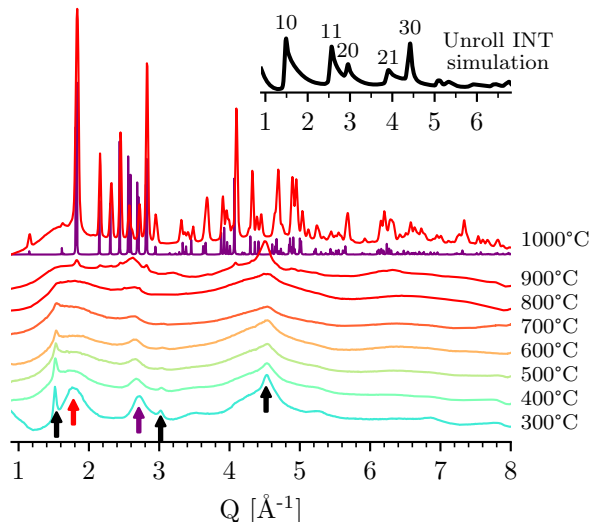

Figure 3: Wide angle X-ray scattering diagrams for powder samples of DW INT, annealed ex-situ up to 1000 °C. Purple diagram is computed from a Ge-mullite structure provided by Voll et al.[53] The inset shows the calculated X-ray scattering diagram of an unrolled imogolite nanotube. Arrows point towards modulations of the form factor of the nanotubes, as discussed in the text.

At room temperature, the diagrams present (i) broad oscillations due to the finite radial dimension of the nanotubes (red and purple arrows in Figure 3 and Figure S2) and (ii) well-defined peaks around Q = 1.5, 3 and 4.5 Å^{-1}

(black arrows). The latter come from the long range periodic order along the nanotube axis. The period is found to be around $8.6\,\text{Å}^{-1}$ for both SW and DW INTs[52].

The evolution of the nanotube period with the temperature will be discussed in more details when presenting in-situ X-ray scattering experiments. However, some conclusions can already be drawn here. For this purpose, we calculated the diffraction diagram of an unrolled imogolite nanotube (inset in Figure 3). Indexes refer to the hexagonal unit cell of the unrolled nanotube (hexagons are drawn in black in Figure 1). The broad modulation around $1.8\,\text{Å}^{-1}$ (red arrow in Figure 3 and Figure S2) is absent in the diffraction diagram of this flat structure. Yet, this component is very present when simulating the X-ray diffraction diagram of an imogolite nanotube.[52] It follows from figures 3 and S2 that such modulation is strongly affected when the temperature increases, while diffraction features characteristic of the hexagonal network persist up to $800\,^\circ\text{C}$. It can thus be inferred than the hexagonal local atomic organization is relatively well maintained upon dehydroxylation, while the tubes are no more circular. Such results had never been reported before.

Above $900\,^\circ\text{C}$, WAXS diagrams of SW and DW INTs are dramatically modified. They exhibit diffraction peaks characteristic of the Ge-mullite structure proposed by Voll et al. (Figure 3).[53] Although the transformation of alumino-silicate nanotubes into mullite at high temperature is well known,[13] this is the first proof that heat-treated GeOH imogolite nanotubes can form Ge-mullite. As evidenced from TGA measurements (Figure 2), formation of mullite is achieved without any mass loss.

The phase transformation of GeOH INTs has also been investigated by infrared spectroscopy (Figure 4 and Figure S3). At room temperature (RT), the IR spectrum of DW imogolite nanotubes presents Ge−O stretching modes, with a characteristic doublet at $805/830\,\text{cm}^{-1}$ (blue arrows in Figure 4) and its shoulder at $915\,\text{cm}^{-1}$, along with a broad absorption band around $555\,\text{cm}^{-1}$ due to Al−O stretching modes.[26,44,51,54] The OH bending vibration of

water molecules is observed at $1635\,\text{cm}^{-1}$ while the broad band near 3000-3800 cm^{-1} is a combination of OH stretching vibrations of INTs, stretching modes of H_2O as well as an overtone of the OH bending mode.[55]
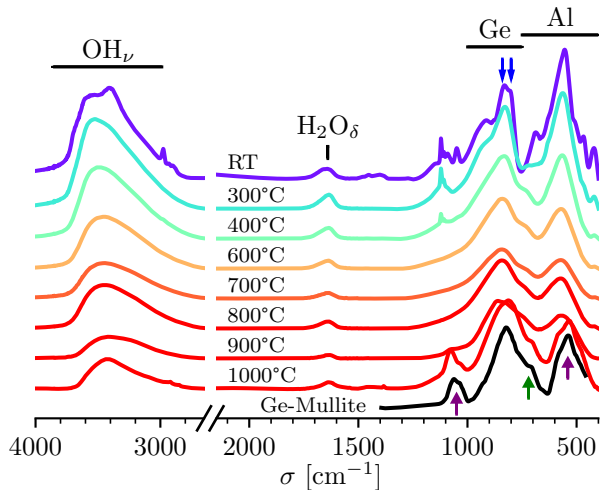

Figure 4: IR absorbance spectra obtained from powders of DW INT, annealed ex-situ up to $1000\,^\circ\text{C}$. The black curve corresponds to synthetic Ge-mullite, adapted from ref.[56]. The blue arrows show a characteristic doublet of the Ge-O stretching vibrations in imogolite nanotubes. The purple and green arrows highlight vibration modes that appear after heat treatment above $900\,^\circ\text{C}$ (see the text).

Significant modifications in the vibrational characteristics of INTs are observed with the heat treatment (Figure 4). Between $300\,^\circ\text{C}$ and $900\,^\circ\text{C}$, the stretching modes associated to aluminum atoms decrease progressively and even vanish due to strong modification of the local structure in the nanotubes. For SW nanotubes, the stretching modes associated with aluminum and the Ge-O stretching vibrations appear to evolve in a similar way (Figure S3). Looking back at DW INTs, we also evidence that the Ge-O stretching contribution shifts to a lower frequency at $1000\,^\circ\text{C}$, while new vibrations modes are observed at 1080 and $540\,\text{cm}^{-1}$ (purple arrows in Figure 4). The peak at $1080\,\text{cm}^{-1}$ can be assigned to the stretching vibration of Ge-O-Ge bonds in the mullite structure.[56] More interestingly, the presence of a significant vibrational contribution at $750\,\text{cm}^{-1}$ (green arrow) should

be mentioned since it is related to bending vibrations of the tetrahedral TO_4 units in the mullite framework.[10,56] The occurrence of this peak upon dehydroxylation, for both SW and DW INTs, indicates that important changes affect the coordination of Al atoms well before re-crystallization in mullite-type compound.

Based on these first insights obtained thanks to ex-situ X-ray sacattering and IR experiments, in-situ experiments have been performed to address the mechanisms of structural transformations of GeOH nanotubes above 300° and before the transformation to mullite, leading to the formation of one or several 'metaimogolite' stages.

Structural investigation of 'meta-imogolite'

Synchrotron experiments were performed on the DiffAbs beamline, which offers the possibility to combine X-ray scattering and X-ray absorption spectroscopy measurements, using the same setup and on the same area of the sample. Figure 5 and Figure S5 show the evolution of XRS diagrams upon heating for all samples.
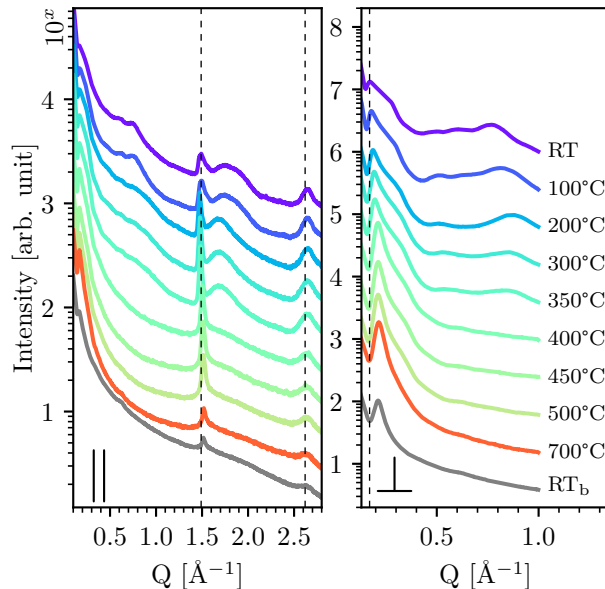

Figure 5: X-ray scattering diagrams measured in parallel (left panel) and perpendicular (right panel) directions to the self-supporting film of DW INTs. XRS measurements were carried out in-situ heat treatment up to 700 °C. The measurement labelled "RT$_b$" (grey curve) refers to the heat-treated sample brought back to room temperature. Curves have been translated for sake of clarity.

In-situ XRS measurements were performed on self-supporting films where the nanotube axes are preferentially in plane. Two non-equivalent X-ray scattering directions are investigated: (i) the direction perpendicular to the film, which provides information on the radial direction of the nanotubes as well as the organization of the nanotubes into bundles; (ii) a direction parallel to the film, which gives structural features along all the directions of the nanotubes (see Figure S4). For instance, peaks related to the period along the nanotubes are only observed in parallel direction. Dashed lines in Figures 5 and S5 are guide for the eye.

The period is calculated from the position of the inflection point of the peak around $1.5 \, \text{Å}^{-1}$, which presents an asymmetric shape as expected for low-dimensional periodic structures.[22,52] It remains unchanged up to T = 400 °C but it shifts towards larger wave-vector values when the temperature is increased. The modulation around $2.5 \, \text{Å}^{-1}$, which can be re-

lated to local hexagonal order (see inset in Figure 3) also shifts towards larger-Q values. The period decrease ($\sim -0.3\,\text{Å}$) corresponds to a shrinking of the nanotubes along their long axis during the dehydroxylation stage. The modulation around $1.8\,\text{Å}^{-1}$ as well as the oscillations for wave-vectors below $1\,\text{Å}^{-1}$ are strongly modified at T = 400 °C. The decrease of the first modulation has already been discussed in terms of radial distortion of the nanotubes. The latter modulations can be calculated within an homogeneous approximation[43,57] and they are also associated with the circular tubular shape. In particular, for DW nanotubes, modulations between $0.5\,\text{Å}^{-1}$ and $1\,\text{Å}^{-1}$ are associated to the interferences between the two nanotube walls. Their disappearance at 400 °C indicates that the two walls are no more concentric and circular. When nanotubes form bundles, XRS diagrams display relatively narrow peaks below $1\,\text{Å}^{-1}$ indexed according to a two-dimensional hexagonal lattice (see red arrows in Figure S5).[41] As evidenced from our experiments, the bundles peaks also disappears when the dehydroxylation starts at T = 300 °C. All these features point towards radial distortions of the nanotubes.

At 700 °C, a small offset of the first scattering peak to $Q_1 \sim 0.15\,\text{Å}^{-1}$ (Figure 5 and S5) is evidenced in all samples. This first modulation of the form factor is still rather intense so that their tubular shape is found to be more or less preserved at 700 °C. The related distance is $d \sim 42\,\text{Å}$ in direct space, close to the value of the outer diameter of both SW and DW nanotube. It may also be noted that for SW and DW bundles, very small intensity peaks are observed at $Q = 2Q_1$ and at $Q = 3Q_1$ at high temperature (see blue arrows in Figure S5). Similar observations were reported for aluminosilicate imogolite nanotubes.[31,33]

The thermal transformation of nanotubes above T = 500 °C is irreversible as shown from the XRS diagrams obtained after return to room temperature (RT_b curves in Figure 5 and S5). Reversibility can only be achieved if the dehydroxylation is not complete.[31,34]

Evolution of the atomic local ordering

To understand how heat-treatment affects the atomic local ordering, we investigated the different samples by using complementary local probes. In a first step, we performed complementary ^{27}Al NMR experiments on GeOH nanotubes before and after ex-situ thermal treatment (T = 800 °C) to identify the different Al coordination environments.

^{27}Al MAS NMR spectra of imogolite nanotubes before heat treatment (Figure 6a and Figure S6) present a main component at 8.8 ppm corresponding to octahedrally coordinated (Al^{VI}) atoms.[15,58] In the case of SW and SW_b samples, this peak presents a chemical shielding anisotropy with a weak contribution at 6.6 ppm. This contribution corresponds to distorted octahedral environments Al_d^{VI}, probably due to wall defects as evidenced previously for aluminosilicate SW INTs.[59] In addition, the ^{27}Al MAS NMR spectrum of SW_b nanotubes display a third minor component (Al^{VI*}) located at ~ 0 ppm, which corresponds to unreacted Al monomers and represents less than 2 % of the Al content.[15]
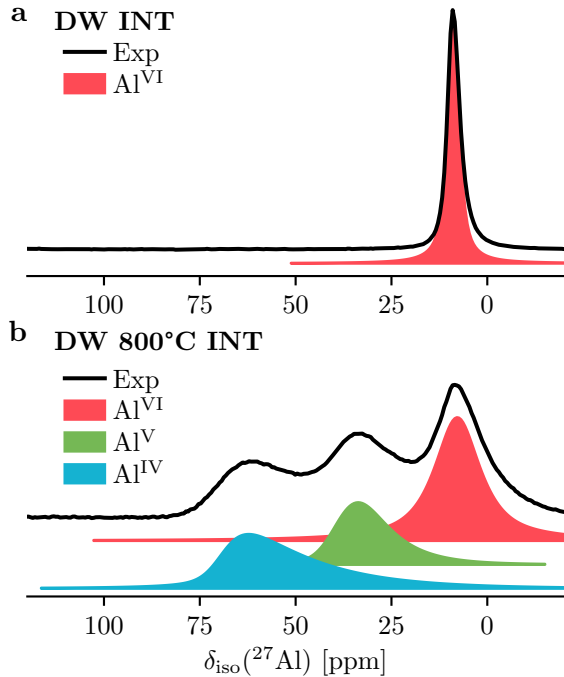
Figure 6: ^{27}Al MAS NMR spectra for a powder of DW INT (a) before and (b) after heat-treatment at 800 °C. Coloured curves correspond to the deconvolution of the experimental black curve.

After heat-treatment at 800°C, the samples show two new well-resolved resonances at 70 ppm and 39 ppm, related to tetrahedral (Al^{IV}) and pentahedral (Al^{V}) environment, respectively (Figure 6b and Figure S7).[32,35,60,61] Furthermore, the chemical shift δ_{iso} of Al^{VI} environment decreases for SW (7.4 ppm) and DW INTs (7.8 ppm). A similar effect was observed for heat-treated aluminosilicate SW INTs,[35] which suggests structural strain with increasing the temperature. However, all these peaks are distributed along the chemical shift line in the ^{27}Al MQMAS spectra with a limited quadrupole-induced shift (Figure S8), allowing one to rule out the presence of multiple Al sites associated with each coordination. The release of hydroxyl groups between 300 and 500 °C implies a decrease of the coordination of Al atoms.[12,32,34,35] The proportion of the different environments around aluminum atoms has been evaluated from a fit of the different components present in the NMR spectra (see Table S1 and Table S2). However, one cannot exclude the possibility of partial rehydroxylation and/or atomic re-arrangement during the cooling step of the samples between heat treatment and NMR measurements.

We investigated in-situ the evolution with temperature of the atomic local ordering thanks to X-ray absorption spectroscopy. Figure 7a and Figure S9 show the variation of the Fourier transform of the k-weighted EXAFS obtained at the Ge K-edge as a function of the temperature. It was measured in conjunction with the X-ray scattering experiments presented previously. The evolution in temperature highlights a decrease in amplitude of the first oscillation combined with a strong attenuation and shift of oscillations beyond $R = 2\,\text{Å}$. The intermediate curves reveal that the effect of heat-treatment on the atomic coordination of Ge atoms is a continuous process.
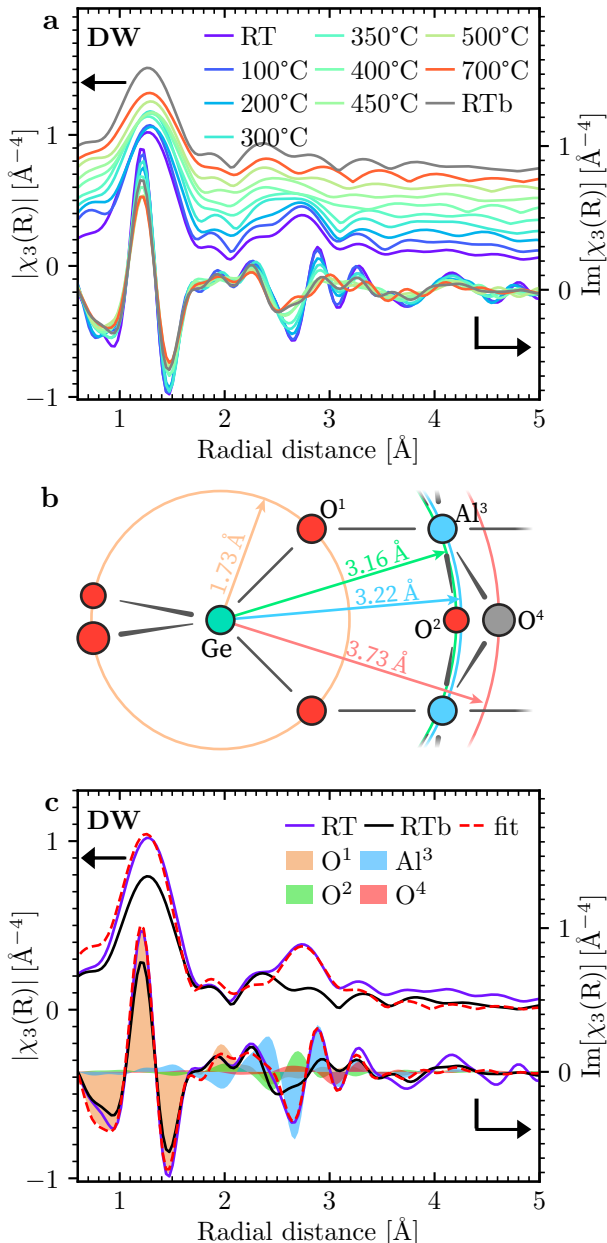
Figure 7: (a) Magnitude (above and shifted for sake of clarity) and imaginary (bellow) part of the Fourier transform (not corrected form phase shift) of the EXAFS $\chi_3(R)$ function collected at the Ge K-edge and for a DW INT powder heated in-situ. (b) Schematic representation of the first four coordination spheres around the scattering atom (Ge). (c) Comparison of EXAFS spectra for unheated INTs (RT) and heat-treated sample brought back to room temperature (RTb) and contribution of the different atomic shells. Red curve corresponds to the best fit of unheated sample.

EXAFS data of the different samples are rather similar, due to their comparable lo-cal structure. Therefore, we started from the imogolite atomic structure inferred from previ-ous WAXS measurements,[52] for which we ex-tracted the backscattering paths. Figure 7b il-lustrates the first four atomic shells around Ge atoms. The backscattering paths were refined to adjust the calculated curves with the exper-imental data. Fit of the EXAFS curve for un-heated INTs allowed us to determine to which atomic shell each oscillation corresponds (Fig-ure 7c and fit parameters in Table S3). This refinement highlights: (1) a first coordination sphere composed of 4 oxygen atoms (O^1) and (2) a second coordination sphere composed of 3 oxygen atoms (O^2), 6 aluminum atoms (Al^3) and 3 external oxygen atoms (O^4). The de-crease of the first atomic shell contribution af-ter heat treatment for RT_b curve is limited and it may be related to some static disor-der. Ge tetrahedral sites are preserved along the thermal decomposition of imogolite nan-otubes. Although the TGA results indicate a complete deshydroxylation, which may be as-sociated with a condensation of Ge atoms with oxygen bridges, as suggested previously for Si-based imogolite nanotubes,[32,34] we do not de-tect an increase in amplitude of the EXAFS function in second atomic shell of germanium atoms.

On the contrary, the amplitude of EXAFS os-cillations are greatly reduced beyond 2 Å. This could be explained by a significant increase of structural disorder starting from the second sphere of coordination. There would be an im-portant spread in the Ge-Ge distances associ-ated with oxygen bridges and a rearrangement of the Al atoms with regard to the Ge ones (see blue area in Figure 7c). A further explana-tion for the reduction of the EXAFS amplitude around 2.7 Å might be that the signal from Al atoms (blue area) is in phase opposition with the signal coming from Ge-O-Ge bridges as il-lustrated in Figure S10.

To complete this investigation, we report on the first in-situ investigation of XAS Al K-edge during the thermal transformation of imogo-lite nanotubes. Flyscan mode allows us to fol-low change in the absorption spectrum with in-creasing the temperature (Figure 8a and Fig-

ure S11). The amplitude of the band around 1572 eV decreases in favour of the lower energy resonance around 1567 eV, similar to what was reported by Andrini et al. for annealed halloysite nanotubes.[11]

To highlight the different components of the absorption spectrum, we draw inspiration from the work of Ildefonse et al.[62,63], who proposed a straightforward deconvolution with a set of Gaussian and a polynomial function, avoiding over-parameterization of the problem. The deconvolution consists of: (i) an arctangent step function for the single aluminum atom absorption component; (ii) a first Gaussian for the absorption of aluminum atoms in Al^{IV} referred as A; (iii) a second Gaussian for the absorption of aluminum atoms in Al^{VI} sites referred as B and (iv) a last Gaussian function to improve the quality of the adjustment in the downward part of the absorption threshold referred as C, related to multiple scattering effects (Figure 8b).[62] It is, however, difficult to discern the footprint of Al^{V} environment, whose contribution is mixed with the one of the Al^{IV} and Al^{VI} sites.[63] A multivariate analysis was also carried out in an effort to identify an Al^{V} component different from Al^{IV} and Al^{VI} ones.[64] No evidence of a distinctive footprint of Al^{V} environment has been found, in agreement with the first approach used.[63]

The particularity of the procedure we put in place is that the refinement was carried out in parallel on the 500 XANES curves for all samples (SW, SW_b, DW and DW_b) as well as on references compounds (Figure 8c and Figure S12). The width and position of the Gaussians are optimized knowing that these parameters are the same over all curves while the amplitude of the Gaussian is refined curve by curve. Gibbsite and kaolinite are used here as six-fold aluminum model compounds with different local structure, the latter being formed by a gibbsite-like sheet linked to a Si tetrahedral one.[63,65] In contrast, mullite corresponds to the final phase expected at the end of the heat treatment (Figure 3) with a relative amount of Al^{VI} and Al^{IV} sites.[66] These references give us benchmarks on the evolution of Al coordination during thermal treatment.

As evidenced in Figure 8c, the local environment around aluminum atoms is altered during the dehydroxylation between 300 and 500 °C followed by a strong decrease of six-fold to four-fold (and/or five-fold) coordinated Al sites in agreement with our previous findings (see A contribution in Figure 8c). Interestingly, the amount of Al sites in the 'metaimogolite' phase obtained at T = 800 °C is closed to the expected structure of a mullite-type compound. The interest of the in-situ experiments compared to the ex-situ ones can be underlined here, as Al^{V} coordination was observed after heat treatment treatment and cooling down of the sample by NMR. Comparison between the different samples reveals some differences in the transition temperature between SW and DW nanotubes while the initial organization of the nanotubes has a limited impact (Figure S12). SW INTs appear to be more sensitive to the thermal treatment, probably due to the presence of distorted octahedral environments in these samples. Finally, we aimed to assess kinetic effects right after dehydroxylation (T = 500 °C) and beyond T = 700 °C during the atomic reorganization. For the latter, there is a slight evolution over time. However, kinetic effects do not appear predominant in the time range we investigated, whatever the samples (Figure S12).

Proposed mechanism of structural reordering during thermal treatment

Thanks to the deconvolution of the XANES spectra, we can identify five steps in the thermal transformation of the local structure around Al atoms as evidenced by insets in Figure 8c. Below T = 300 °C, aluminum remains only in Al^{VI} form. Up to 500 °C, the decrease in the coordination of Al atoms is related to dehydroxylation effects in accordance with TGA measurements. In the range 500-600 °C, aluminum coordination remains stable. However, the proportion of Al^{VI} sites drops significantly between 600 and 800 °C. Above 800 °C, the local structure around the aluminum atoms no longer evolves.

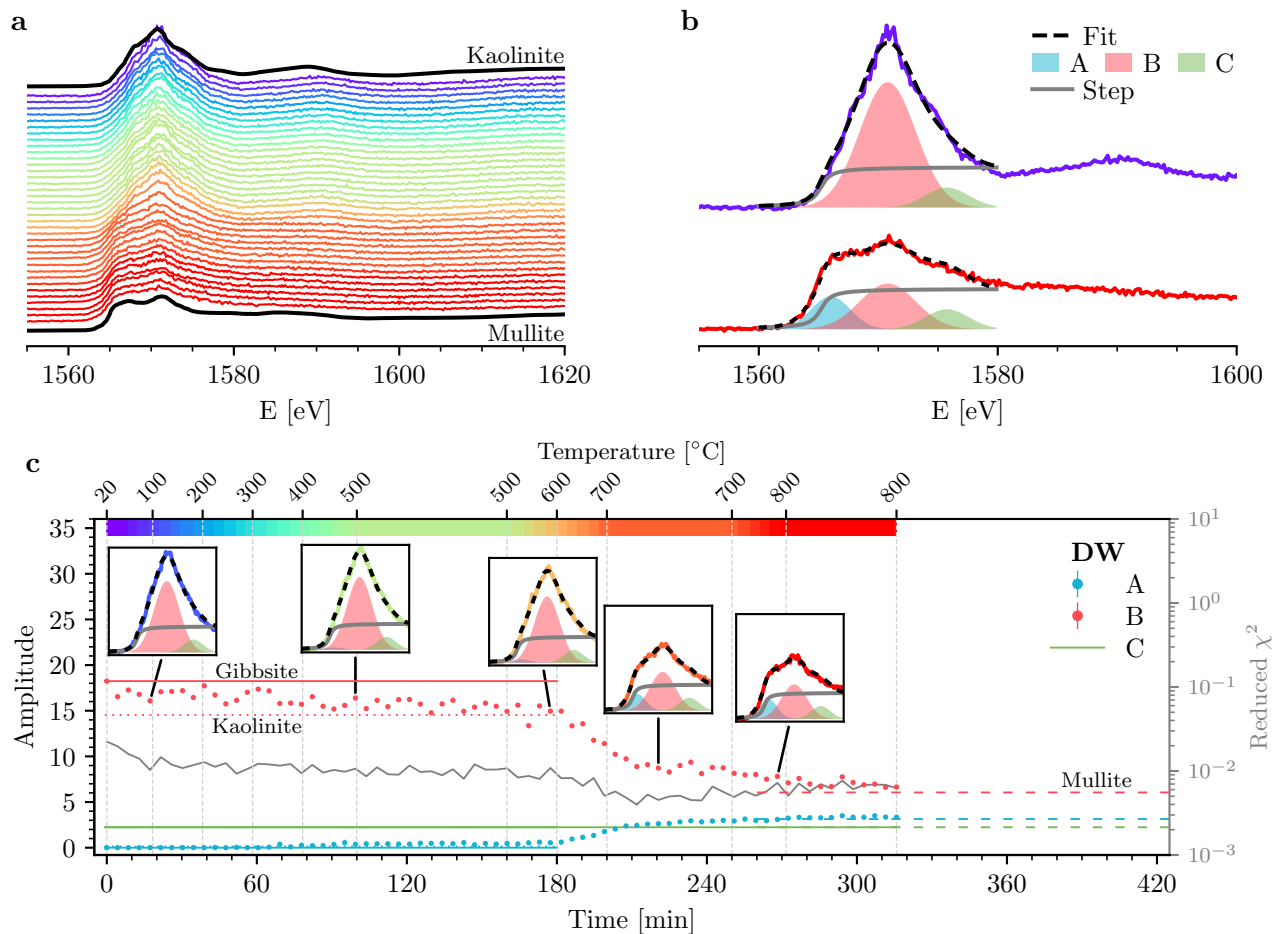Interestingly, the modification of aluminum

Figure 8: (a) Al K-edge XANES spectra series measured for a DW powder heated in-situ from ambient temperature (purple curve) to 800°C (red curve). (b) Typical refinement of the absorption threshold by 3 Gaussian components and a step-like function for the first (RT) and last XANES curve (T = 800 °C) of the series. (c) Amplitude of the first, the second and the third fitting Gaussians over heat treatment. The temperature and the time are displayed, respectively, on the top-axis and the bottom axis to reveal kinetic effect. The goodness of fit (reduced χ^2) is drawn as grey curve. In addition, Gaussian components of the fitting procedure are given for different reference samples: gibbsite (full line), kaolinite (dotted line) and Si-mullite (dashed line).

coordination takes place in two separate steps but the dehydroxylation one contributes the least to the variation of the XANES spectra. The only possible explanation is that dehydroxylation leads to the formation of exclusively pentahedral aluminum Al^V, which contribute largely to the B component at approximately 1570 eV in the deconvolution. The second step of modification of the XANES data (T = 600-800 °C) reflects the formation of tetrahedral aluminum, as evidenced by the rise in component A at the expense of component B. Such modification of the structure takes place after the removal of hydroxyl groups, at constant mass

(according to TGA data). Therefore, the appearance of Al^{IV} must be accompanied by a local structural reordering with the formation of Al^{VI} from Al^V (Figure 9). Above 800 °C, we no longer observe any change in the coordination of Al atoms in the final structures.

Altogether, the combination of our observations leads us to propose a novel mechanism on the thermal transformation of GeOH imogolite nanotubes (Figure 9):

1. Dehydroxylation of INTs occurs between 300 and 500 °C with the formation of Al^V to the detriment of Al^{VI}. Altogether,

this leads to radial distortions of the nanotubes.

2. Between 500 and 600 °C, dehydroxylated structures form a metaimogolite phase (Stage I) composed of Al^V and Al^{VI} sites.

3. For temperature in the range 600-800 °C, a peculiar atomic reorganization takes place in the metaimogolite structure (Stage II), where the Al^V disappear in favor of Al^{IV} and Al^{VI} by a possible atomic jump process ($Al^V + Al^V \longrightarrow Al^{VI} + Al^{IV}$).

4. The metaimogolite phase obtained at T = 800 °C remains relatively unaffected up to ~ 1000 °C (Stage III), where the elementary bricks Al^{VI} and Al^{IV} then reorganize into a mullite-type structure.
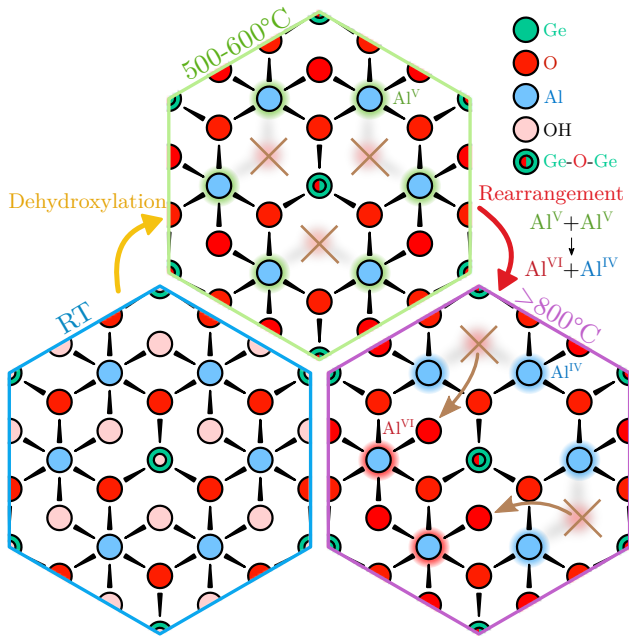

Figure 9: Scheme of dehydroxylation of imogolite nanotubes leading to a transformation of the octahedral configurations Al^{VI} into Al^V and Al^{IV} configuration. The hexagons are associated with 2 unit cells of imogolite nanotube $2\,[(OH)_3Al_2O_3Ge(OH)]$. The black lines indicate the interatomic bonds. Brown crosses show hydroxyl groups and bonds lost during dehydroxylation.

Conclusion

We investigated the thermal stability of SW and DW aluminogermanate INTs over a wide range of temperature. The combination of local techniques (IR, NMR and XAS spectroscopies) and of X-ray scattering allowed us to probe at the atomic scale the fate of Al and Ge atoms coordination during thermal treatment as well as the modification of the nanotube period and shape. The strength of this work is associated with the use of in-situ experiments. Beyond the dehydroxylation of the nanotubes and the re-crystallization into a mullite-type compound, our experiments provided new insights on the mechanisms involved in the formation of intermediate metaimogolite states formed in the range of temperature (T = 300-800 °C). After dehydroxylation, a first metaimogolite structure is formed by release of hydroxyl groups leading to Al^V sites with important changes in the nanotube shape. Major atomic reorganization of this phase occur between 500 and 600 °C (stage II), probably by atomic jump processes. A decrease in periodicity of the metaimogolite compound is observed and the tubes have no longer circular cross-sections. The structure of the resulting metaimogolite phase (stage III) does not evolve until re-crystallization into a Ge-mullite type compound at T > 900 °C. The understanding of the structural modifications of GeOH nanotubes as a function of temperature represents a benchmark for further studies concerning the reactivity of these metaimogolite phases.

Supporting Information Available

Additional thermogravimetric analysis, X-ray scattering, NMR measurements, EXAFS at the Ge K-edge and XANES at the Al K-edge for imogolite nanotubes with one or two walls, isolated or in bundles.

References

(1) Heller-Kallai, L. *Developments in Clay Science*; Elsevier, 2006; Vol. 1; pp 289–308.

(2) Brindley, G. W.; Nakahira, M. *Journal of the American Ceramic Society* **1959**, *42*, 311–314.

(3) Bellotto, M.; Gualtieri, A.; Artioli, G.; Clark, S. M. *Physics and chemistry of minerals* **1995**, *22*, 207–217.

(4) Muraleedharan, M. G.; Asgar, H.; Mohammed, S.; Gadikota, G.; van Duin, A. C. T. *Chemistry of Materials* **2020**, *32*, 651–662.

(5) Daou, I.; Lecomte-Nana, G. L.; Tessier-Doyen, N.; Peyratout, C.; Gonon, M. F.; Guinebretiere, R. *Minerals* **2020**, *10*, 480.

(6) Lenarda, M.; Storaro, L.; Talon, A.; Moretti, E.; Riello, P. *Journal of colloid and interface science* **2007**, *311*, 537–543.

(7) Sabir, B. B.; Wild, S.; Bai, J. *Cement and Concrete Composites* **2001**, *23*, 441–454.

(8) Belver, C.; Bañares Muñoz, M. A.; Vicente, M. A. *Chemistry of Materials* **2002**, *14*, 2033–2043.

(9) Chandrasekhar, S.; Pramada, P. N. *Microporous and Mesoporous Materials* **2008**, *108*, 152–161.

(10) Yuan, P.; Tan, D.; Annabi-Bergaya, F.; Yan, W.; Fan, M.; Liu, D.; He, H. *Clays and Clay Minerals* **2012**, *60*, 561–573.

(11) Andrini, L.; Moreira Toja, R.; Conconi, M. S.; Requejo, F. G.; Rendtorff, N. M. *Journal of Electron Spectroscopy and Related Phenomena* **2019**, *234*, 19–26.

(12) Du, P.; Yuan, P.; Liu, D.; Wang, S.; Song, H.; Guo, H. *Applied Clay Science* **2018**, *158*, 211–218.

(13) Yoshinaga, N.; Aomine, S. *Soil Science and Plant Nutrition* **1962**, *8*, 22–29.

(14) Mukherjee, S.; Bartlow, V. M.; Nair, S. *Chemistry of Materials* **2005**, *17*, 4900–4909.

(15) Levard, C.; Rose, J.; Thill, A.; Masion, A.; Doelsch, E.; Maillet, P.; Spalla, O.; Olivi, L.; Cognigni, A.; Ziarelli, F.; et al., *Chemistry of Materials* **2010**, *22*, 2466–2473.

(16) Yucelen, G. I.; Choudhury, R. P.; Vyalikh, A.; Scheler, U.; Beckham, H. W.; Nair, S. *Journal of the American Chemical Society* **2011**, *133*, 5397–5412.

(17) Kang, D.-Y.; Brunelli, N. A.; Yucelen, G. I.; Venkatasubramanian, A.; Zang, J.; Leisen, J.; Hesketh, P. J.; Jones, C. W.; Nair, S. *Nature communications* **2014**, *5*, 1–9.

(18) Amara, M. S.; Paineau, E.; Rouzière, S.; Guiose, B.; Krapf, M.-E. M.; Taché, O.; Launois, P.; Thill, A. *Chemistry of Materials* **2015**, *27*, 1488–1494.

(19) Paineau, E.; Krapf, M.-E. M.; Amara, M.-S.; Matskova, N. V.; Dozov, I.; Rouzière, S.; Thill, A.; Launois, P.; Davidson, P. *Nature Communications* **2016**, *7*, 10271.

(20) Thill, A.; Picot, P.; Belloni, L. *Applied Clay Science* **2017**, *141*, 308–315.

(21) Picot, P.; Liao, Y.; Barruet, E.; Gobeaux, F.; Coradin, T.; Thill, A. *Langmuir* **2018**, *34*, 13225–13234.

(22) Monet, G.; Amara, M. S.; Rouzière, S.; Paineau, E.; Chai, Z.; Elliott, J. D.; Poli, E.; Liu, L.-M.; Teobaldi, G.; Launois, P. *Nature communications* **2018**, *9*, 1–9.

(23) Paineau, E. *Applied Sciences* **2018**, *8*, 1921.

(24) Cradwick, P. D. G.; Farmer, V. C.; Russell, J. D.; Masson, C. R.; Wada, K.; Yoshinaga, N. *Nature Physical Science* **1972**, *240*, 187–189.

(25) Paineau, E.; Launois, P. *Nanomaterials from Clay Minerals*; Elsevier, 2019; pp 257–284.

(26) Maillet, P.; Levard, C.; Larquet, E.; Mariet, C.; Spalla, O.; Menguy, N.; Masion, A.; Doelsch, E.; Rose, J.; Thill, A. *Journal of the American Chemical Society* **2010**, *132*, 1208–1209.

(27) Thill, A.; Maillet, P.; Guiose, B.; Spalla, O.; Belloni, L.; Chaurand, P.; Auffan, M.; Olivi, L.; Rose, J. *Journal of the American Chemical Society* **2012**, *134*, 3780–3786.

(28) Rouzière, S.; Amara, M. S.; Paineau, E.; Launois, P. *Developments in Clay Science*; Elsevier, 2016; Vol. 7; pp 254–278.

(29) Donkai, N.; Miyamoto, T.; Kokubo, T.; Tanei, H. *J. Mater. Sci.* **1992**, *27*, 6193–6196.

(30) Farmer, V. C.; Adams, M. J.; Fraser, A. R.; Palmieri, F. *Clay Miner.* **1983**, *18*, 459–472.

(31) Van der Gaast, S. J.; Wada, K.; Wada, S.-I.; Kakuto, Y. *Clays and Clay Minerals* **1985**, *33*, 237–243.

(32) MacKenzie, K. J. D. *Clays and Clay Minerals* **1989**, *37*, 317–324.

(33) Zanzottera, C.; Vicente, A.; Armandi, M.; Fernandez, C.; Garrone, E.; Bonelli, B. *J. Phys. Chem. C* **2012**, *116*, 23577–23584.

(34) Kang, D.-Y.; Zang, J.; Wright, E. R.; McCanna, A. L.; Jones, C. W.; Nair, S. *Acs Nano* **2010**, *4*, 4897–4907.

(35) Hatakeyama, M.; Hara, T.; Ichikuni, N.; Shimazu, S. *Bulletin of the Chemical Society of Japan* **2011**, *84*, 656–659.

(36) Wilson, M. A.; Wada, K.; Wada, S. I.; Kakuto, Y. *Clay minerals* **1988**, *23*, 175–190.

(37) da Silva, M. C.; dos Santos, E. C.; Lourenço, M. P.; Gouvea, M. P.; Duarte, H. A. *Frontiers in Materials* **2015**, *2*, 16.

(38) Antoni, M.; Rossen, J.; Martirena, F.; Scrivener, K. *Cement and Concrete Research* **2012**, *42*, 1579–1589.

(39) Zapała-Sławeta, J. *Materials and Structures* **2017**, *50*.

(40) Amara, M.-S.; Paineau, E.; Bacia-Verloop, M.; Krapf, M.-E. M.; Davidson, P.; Belloni, L.; Levard, C.; Rose, J.; Launois, P.; Thill, A. *Chemical Communications* **2013**, *49*, 11284–11286.

(41) Paineau, E.; Amara, M. S.; Monet, G.; Peyre, V.; Rouzière, S.; Launois, P. *The Journal of Physical Chemistry C* **2017**, *121*, 21740–21749.

(42) Paineau, E.; Monet, G.; Peyre, V.; Goldmann, C.; Rouzière, S.; Launois, P. *Langmuir* **2019**,

(43) Amara, M. S.; Rouzière, S.; Paineau, E.; Bacia-Verloop, M.; Thill, A.; Launois, P. *The Journal of Physical Chemistry C* **2014**, *118*, 9299–9306.

(44) Paineau, E.; Rouzière, S.; Monet, G.; Diogo, C. C.; Morfin, I.; Launois, P. *Journal of Colloid and Interface Science* **2020**,

(45) Liao, Y.; Picot, P.; Lainé, M.; Brubach, J.-B.; Roy, P.; Thill, A.; Le Caër, S. *Nano Research* **2018**, 4759–4773.

(46) Amara, M. S. Nanotubes d'imogolite et propriétés de l'eau confinée : organisation, structure et dynamique. Theses, Université Paris Sud - Paris XI, 2014.

(47) Massiot, D.; Fayon, F.; Capron, M.; King, I.; Le Calvé, S.; Alonso, B.; Durand, J.-O.; Bujoli, B.; Gan, Z.; Hoatson, G. *Magnetic Resonance in Chemistry* **2002**, *40*, 70–76.

(48) Ravel, B.; Newville, M. *Journal of Synchrotron Radiation* **2005**, *12*, 537–541.

(49) Vantelon, D.; Trcera, N.; Roy, D.; Moreno, T.; Mailly, D.; Guilet, S.; Metchalkov, E.; Delmotte, F.; Lassalle, B.; Lagarde, P.; et al., *Journal of Synchrotron radiation* **2016**, *23*, 635–640.

(50) Newville, M. et al. LMfit: Non-Linear Least-Square Minimization and Curve-Fitting for Python. 2019.

(51) Liao, Y.-Y.; Picot, P.; Brubach, J.-B.; Roy, P.; Thill, A.; Le Caer, S. *The Journal of Physical Chemistry C* **2019**, *123*, 19768–19777.

(52) Monet, G.; Paineau, E.; Chai, Z.; Amara, M. S.; Orecchini, A.; Jiménez-Ruiz, M.; Ruiz-Caridad, A.; Fine, L.; Rouzière, S.; Liu, L.-M.; et al., *Nanoscale Advances* **2020**, *2*, 1869–1877.

(53) Voll, D.; Lengauer, C.; Beran, A.; Schneider, H. *European Journal of Mineralogy* **2001**, *13*, 591–604.

(54) Wada, S.-i.; Wada, K. *Clays and Clay Minerals* **1982**, *30*, 123–128.

(55) Bishop, J. L.; Ethbrampe, E. B.; Bish, D. L.; Abidin, Z. L.; Baker, L. L.; Matsue, N.; Henmi, T. *Clays and Clay Minerals* **2013**, *61*, 57–74.

(56) Voll, D.; Angerer, P.; Beran, A.; Schneider, H. *Vibrational Spectroscopy* **2002**, *30*, 237–243.

(57) Cambedouzou, J.; Chorro, M.; Almairac, R.; Noé, L.; Flahaut, E.; Rols, S.; Monthioux, M.; Launois, P. *Physical Review B* **2009**, *79*, 195423.

(58) Goodman, B. A.; Russell, J. D.; Montez, B.; Oldfield, E.; Kirkpatrick, R. J. *Physics and Chemistry of Minerals* **1985**, *12*, 342–346.

(59) Yucelen, G. I.; Choudhury, R. P.; Leisen, J.; Nair, S.; Beckham, H. W. *The Journal of Physical Chemistry C* **2012**, *116*, 17149–17157.

(60) Woessner, D. E. *American Mineralogist* **1989**, *74*, 203–215.

(61) Smith, M. E. *Applied Magnetic Resonance* **1993**, *4*, 1–64.

(62) Ildefonse, P.; Kirkpatrick, R. J.; Montez, B.; Calas, G.; Flank, A. M.; Lagarde, P. *Clays and Clay Minerals* **1994**, *42*, 276–287.

(63) Ildefonse, P.; Cabaret, D.; Sainctavit, P.; Calas, G.; Flank, A.-M.; Lagarde, P. *Physics and Chemistry of Minerals* **1998**, *25*, 112–121.

(64) Cassinelli, W. H.; Martins, L.; Passos, A. R.; Pulcinelli, S. H.; Santilli, C. V.; Rochet, A.; Briois, V. *Catalysis Today* **2014**, *229*, 114–122.

(65) Kato, Y.; Shimizu, K.-i.; Matsushita, N.; Yoshida, T.; Yoshida, H.; Satsuma, A.; Hattori, T. *Physical Chemistry Chemical Physics* **2001**, *3*, 1925–1929.

(66) Schneider, H.; Schreuer, J.; Hildmann, B. *Journal of the European Ceramic Society* **2008**, *28*, 329–344.

Graphical TOC Entry